International Journal of Heat and Mass Transfer 255 (2026) 127802

Contents lists available at ScienceDirect

International Journal of Heat and Mass Transfer

journal homepage: www.elsevier.com/locate/ijhmt

Multiscale analysis of heat-mass-reaction coupling in the controlled synthesis of graphene oxide via heart-shaped microchannels

Yifan Li [a,b], Xiaojun Xiong [a], Hongao Yang [b], Wei Yu [a], Bingyang Cao [b,*]

[a] School of Energy and Materials, Shanghai Polytechnic University, Shanghai 201209, China
[b] Key Laboratory for Thermal Science and Power Engineering of Ministry of Education, Department of Engineering Mechanics, Tsinghua University, Beijing 100084, China

ARTICLE INFO

Keywords:
Heat transfer
Microchannel
Discrete phase model
Discrete element method
Reactive molecular dynamics

ABSTRACT

Precise regulation of the oxidation degree of graphene oxide (GO) is critical for tailoring its physicochemical properties and expanding its applications. In this work, a heart-shaped microchannel was designed to achieve controlled GO synthesis via geometry-induced heat-mass-reaction coupling. A multiscale simulation strategy integrating the Discrete Phase Model (DPM), Discrete Element Method (DEM), and Reactive Molecular Dynamics (RMD) was developed to uncover the underlying mechanism. Increasing the inlet velocity from 0.025 m/s to 1.0 m/s enhanced the maximum shear rate and wall heat flux, accelerating convective heat transfer and mass mixing in the bifurcation and recombination zones. The higher flow velocities induced stronger interparticle and wall contact forces, potentially facilitating graphite fragmentation. Experimental results demonstrated that as the flow velocity decreases (from 1.0 m/s to 0.025 m/s), the O/C ratio decreases from 0.44 to 0.21, showing good agreement with the oxidation trend predicted by the RMD simulations (from 0.43 to 0.28). This study establishes a geometry-guided, multiphysics-multiscale framework for the rational design of microchannel systems for nanomaterial synthesis.

1. Introduction

Graphene oxide (GO), a two-dimensional carbon material with a rich structural composition and high chemical reactivity, has demonstrated broad application potential in fields such as flexible electronics, energy storage, catalysis, and biomedicine [1–4]. The performance of GO is highly dependent on its degree of oxidation, including the type, distribution, and content of oxygen-containing functional groups [5,6]. At the same loading level, GO with different degrees of oxidation often exerts markedly distinct effects on the properties of the resulting composites [7]. Therefore, precise control over the oxidation level is critical for the rational design and fabrication of functionalized graphene-based materials. Conventional methods for the synthesis of GO primarily rely on liquid-phase chemical oxidation, such as the Hummers method and its derivatives [8,9]. Marcano et al. enhanced the oxidation efficiency of the conventional Hummers method by increasing the dosage of $KMnO_4$ and conducting the reaction in a 9:1 mixture of H_2SO_4 and H_3PO_4 [10]. Building on the improved Hummers protocol, Huang et al. adopted a one-pot long-duration stirring oxidation approach, which led to highly oxidized graphite and the production of GO sheets with large lateral dimensions and high surface areas [11]. Chen et al. optimized the Hummers method by reducing the use of $NaNO_3$, thereby eliminating the emission of toxic NO_2/N_2O_4 gases and streamlining wastewater treatment without sacrificing the product yield [12]. However, the above-mentioned approaches often suffer from several limitations, including longer reaction times, non-uniform oxidation, and poor controllability. This fundamental limitation arises from the lack of precise control over local reaction environments (such as temperature, shear, and mass transport) in conventional liquid-phase systems, necessitating the integration of microchannel technologies that offer spatiotemporal tunability to overcome these constraints.

Microchannel technology was initially developed for thermal management applications. Liu et al. introduced horizontal and inclined fin structures into a dual-layer microchannel and proposed a nested dual-layer impinging jet microchannel heat sink, which reduced the substrate temperature by 11.30 K, enhanced the Nusselt number by 62.11 %, and improved the overall heat transfer performance by 18.02 % at $Re = 165.84$ [13]. Sun et al. employed variable-density topology optimization to design multiple inlet-outlet configurations combining parallel flow and jet structures, and observed that with increasing jet ratio, the

* Corresponding author.
E-mail address: caoby@tsinghua.edu.cn (B. Cao).

https://doi.org/10.1016/j.ijheatmasstransfer.2025.127802
Received 16 June 2025; Received in revised form 7 August 2025; Accepted 2 September 2025

flow behavior transitioned from parallel to jet-dominated, resulting in a decline in heat transfer performance [14]. Zhuo et al. developed a microchannel heat sink integrating dual-layer nesting, impinging jet, and bifurcation structures, achieving a composite heat transfer coefficient as high as 1.355 and demonstrating superior thermal dissipation performance [15]. Building upon this design, Shen et al. incorporated central fins, flow blocks, and vertical bifurcation structures into the system through a combination of numerical simulation and 3D printing, and systematically identified the optimal configuration and dimensional parameters [16–18].

Recently, microchannel technology has been increasingly adopted in chemical synthesis due to its advantages in mass transfer enhancement, reduced reaction time, and improved process controllability [19,20]. Moreover, the microchannel provides an effective platform for observing the thermal behavior of particles in fluid environments [21]. Zhu et al. investigated the flow behavior, gas-liquid distribution, and mass transfer characteristics of CO_2 absorption in sodium glycinate aqueous solution within parallel multichannel microreactors using a high-speed camera, demonstrating that multichannel microreactors exhibit excellent flow uniformity and mass transfer performance [22]. Hao et al. achieved the controlled encapsulation of phase change materials (PCMs) into individual microcapsules, enabling precise control over capsule size and core-to-shell ratio (i.e., temperature regulation capacity) by adjusting the flow rates of the inner and outer phases [23,24]. Rafique et al. designed a straight microchannel reactor for the synthesis of silver-chitosan nanocomposites, enabling control over the particle size distribution [25]. Although such linear microchannel structures are simple and easy to fabricate, their flow profiles are typically limited to laminar regimes, leading to insufficient mixing and, consequently, non-uniform oxidation [26]. Kim et al. developed a blade-shaped microfluidic channel integrated with an embedded solution-shearing technique [27]. This configuration enabled ultrafast ($\leq$5 mm/s) and large-area synthesis of conductive metal-organic framework films embedded with high-quality nanocatalysts. While this approach improved reaction uniformity to a certain extent, it still faced challenges such as limited mixing zones and non-uniform shear gradient distribution, making it difficult to finely regulate particle behavior at the microscale. Han et al. introduced a vortex-focused microfluidic device that generated intense vortices around axisymmetric lipid flows using two conical microchannels [28]. This system enabled rapid convective and diffusive mixing between lipid and buffer streams, offering precise control over residence time and reaction environment. It should be mentioned that such configurations often require complex pumping systems and flow control mechanisms, and may be prone to particle sedimentation or clogging in solid-liquid systems such as graphite-sulfuric acid reactions. Chai et al. incorporated a valve-assisted mixer at the intersection of two microchannels to achieve rapid mixing of positively charged chitosan and negatively charged lignin solutions [29]. The electrostatic co-assembly between amino groups in chitosan and carboxyl groups in lignin facilitated the rapid formation of structurally tunable lignin-chitosan nanoparticles. Although various microchannel designs have been successfully applied in the synthesis of nanomaterials, most of these are tailored for liquid-liquid systems and offer limited control over particle dynamics in solid-liquid reactions [30]. Therefore, these existing designs fall short of meeting the specific demands of GO synthesis, which requires precise control over local shear enhancement, heat and mass transfer efficiency, and oxidation degree. This highlights the urgent need to develop a microchannel structure capable of generating high shear disturbances and providing a tunable reaction environment, thereby enabling fine regulation of particle behavior and oxidation level during GO synthesis.

A novel heart-shaped microchannel structure was designed in this study to enhance fluid mixing efficiency through its unique vortex-inducing effect. Compared with conventional straight or serpentine channels, this configuration more effectively facilitates interlayer intercalation of graphite and diffusion of oxidants, offering the potential to overcome the kinetic limitations of the oxidation process [31]. The periodic bifurcation-recombination design continuously induces shear and perturbation on the particles during flow, thereby significantly enhancing local mixing and reaction uniformity. Simultaneously, the system allows for tunable residence time and localized force fields, enabling the rapid and controllable synthesis of GO with well-regulated oxidation degrees. To understand the underlying mechanisms, a comprehensive multiphysics-multiscale simulation strategy was developed, integrating macroscopic particle flow modeling, microscale particle mechanics, and atomistic-level reaction simulations. This approach provides a theoretical framework for understanding the formation mechanism of oxidation-controlled GO. The results revealed that the locally induced shear and pressure gradient fields within the microchannel are the key factors governing particle stress distribution and reaction pathways. The simulation results and proposed reaction mechanism were experimentally validated by X-ray photoelectron spectroscopy (XPS) analysis of GO samples synthesized under different flow rates, confirming both the reliability of the model and the accuracy of the mechanistic interpretation.

2. Modeling principle and numerical analysis method

2.1. Practical experimental setup and geometric models

This study investigates solid-liquid reactions within a heart-shaped microchannel of fixed dimensions, focusing on how varying inlet flow velocities influence heat and mass transfer between solid particles and the solution, thereby affecting the oxidation degree of the resulting GO. Different inlet velocities are tried: 0.025 m/s, 0.1 m/s, 0.25 m/s, 0.5 m/s, and 1 m/s. The schematic illustration of the synthesis process of GO via a 7 $\times$ 8 heart-shaped microchannel is shown in Fig. 1a. The digital image and component composition of the physical object are shown in **Figure S1.** Fig. 1b presents the key planar dimensions of the heart-shaped microchannel, which was fabricated on a 120 mm $\times$ 120 mm glass via an etching process. Fig. 1c schematically illustrates the spatial motion of graphite flakes and the shear rate distribution within the microchannel, while the motion behavior of graphite flakes within the microchannel was captured using a high-speed camera, as shown in Fig. 1d It should be noted that the oxidation process was completed within 0.5 h, which is approximately 75 % faster than the straight-through microchannel system (e.g., >2 h for CO_2 absorption in Ref. [16]) and over 92 % shorter than the conventional Hummers' method.

2.2. Numerical analysis method

Liquid-solid multiphase flow involves complex interactions between the fluid and solid particles, encompassing fluid dynamics, particle collisions, heat and mass transfer, and particle fragmentation [32]. The Discrete Phase Model (DPM) is commonly employed, which treats particle swarms as quasi-continuous or adjustable fluids under a one-way coupling framework [33]. It has the advantages of high computational efficiency through direct utilization of high-resolution flow field data and intuitive visualization of particle trajectories. However, it fails to capture complex inter-particle collisions and friction and is thus inadequate for modeling particle fragmentation and agglomeration as required in this study. The Discrete Element Method (DEM) treats each particle as an individual discrete entity and calculates particle motion and interactions. By accurately accounting for contact mechanics between particles and between particles and channel walls, DEM enables precise simulation of particulate dynamics. In this study, DPM is utilized to capture the macroscopic flow trajectories of particles, while DEM is introduced to investigate the stress states associated with fragmentation and related behaviors [34]. Specifically, the background flow field (e.g., velocity, pressure, temperature) is provided by ANSYS Fluent, while Rocky is employed to perform detailed modeling of particle-scale

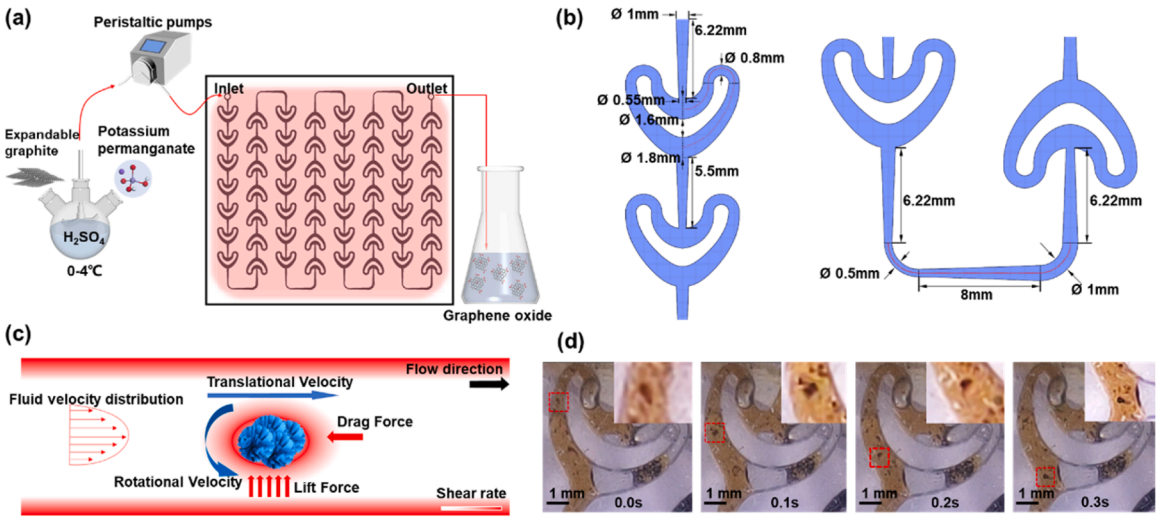

Fig. 1. (a) Schematics of the experiment setup employed in the microfluidic synthesis of GO and the enlarged microchannel setup; (b) The detailed dimensions of the adjacent microchannel; (c) The spatial motion of graphite flakes and the shear rate distribution within the microchannel; (d) The recorded motion behavior of graphite flakes within the microchannel.

behaviors (e.g., motion, collision, and fragmentation) based on this flow field. Data exchange between the two solvers is achieved via a CFD-DEM coupling interface, synchronizing the flow field and particle information at each time step to yield force field data within the microchannel. The obtained stress states and contact forces are used as boundary loads or initial conditions to simulate bond rupture (oxidation) in localized fracture regions using Reactive Molecular Dynamics (RMD), providing atomistic-level insights into material behavior and offering theoretical support for the observed experimental phenomena. The simulation of the continuous phase flow field, along with particle behaviors such as motion, collision, rotation, and fragmentation, as well as particle-fluid heat exchange, shear-induced thermal flux, microscale force responses, bond breakage, and functional group transformations, is not an independent process. Instead, they are interrelated and coupled through interface protocols and data exchange mechanisms, collectively influencing one another. Accordingly, the mechanistic investigations in this study are conducted using a Multiphysics-Multiscale coupled simulation strategy.

2.2.1. DPM model

A dual-medium simulation framework is employed to investigate the characteristics of solid-liquid mixed flow. The particle phase is modeled as a quasi-continuous or deformable fluid. Considering the microscale dimensions of the channel, the fluid flow is solved using a laminar flow model [35]. Based on the Euler-Lagrange approach, the continuity equation for the liquid phase is established, incorporating the momentum conservation law. The mathematical model describing its flow behavior is expressed as follows, Eqs. (1–3):

$$\frac{\partial}{\partial t}(\alpha_f \rho_f) + \nabla(\alpha_f \rho_f u_f) = 0 \tag{1}$$

$$\frac{\partial}{\partial t}(\alpha_f \rho_f u_f) + \nabla(\alpha_f \rho_f u_f u_f) = -\alpha_f \nabla p + \alpha_f \nabla \tau_f + \alpha_f \rho_f g \tag{2}$$

$$\frac{\partial}{\partial t}(\alpha_f \rho_f E_f) + \nabla(\alpha_f \rho_f E_f u_f) = -\nabla(\alpha_f \tau_f \cdot u_f) + \alpha_f \rho_f g \cdot u_f - \nabla q_f + Q_f \tag{3}$$

α_f is the volume fraction of the fluid, ρ_f is the density of the fluid, and u_f is the velocity of the fluid. p is the pressure, τ_f is the stress tensor of the fluid, and g is the acceleration of gravity. E_f is the overall energy of the fluid, calculated by $E_f = e_f + \frac{1}{2}|u_f{}^2|$, q_f is the heat flux density, calculated by $q_f = -k_f \nabla T$ (k_f is the thermal conductivity of the fluid), and Q_f is the heat source.

The trajectory of discrete phase particles is predicted by integrating the force balance acting on each particle, formulated in a Lagrangian reference frame. This force balance equates the particle inertia to the sum of forces acting on it, Eq. (4):

$$m_p \frac{\partial u_p}{\partial t} = m_p \frac{u - u_p}{\tau_r} + m_p \frac{g(\rho_p - \rho)}{\rho_p} + F \tag{4}$$

m_p is the mass of the particle, u_p is the velocity of the particle, τ_r is the relaxation time, ρ_p is the density of the particle, and F is the attached force. The wall surfaces were assigned a constant temperature of 310 K. Although constant wall temperature is an idealized condition, it was adopted here to isolate the effect of inlet velocity on heat and mass transfer. This simplification facilitates comparative analysis and avoids added complexity from variable wall temperatures. The fluid phase was modeled using the physical properties of concentrated sulfuric acid, while the discrete phase represented graphite-based intercalation compounds formed by the reaction of graphite with sulfuric acid and potassium permanganate, as summarized in Table 1. The particle diameter was uniformly set to 40 μm. The conical inlet of the first heart-shaped microchannel unit was defined as the inlet for a solid-liquid mixture at a temperature of 275 K, with an inlet velocity varying from 0.025 m/s to 1 m/s. The outlet was defined as a pressure outlet with a gauge pressure of 0 Pa. All external surfaces of the microchannel were assumed to be adiabatic, and the channel walls were modeled as glass. A laminar flow model was used with a pressure-velocity coupling algorithm. Second-order upwind schemes were applied to the discretization of the continuity, momentum, energy, and laminar flow equations. The simulation was considered converged when the residuals of the continuity, momentum, and turbulence dissipation equations fell below 10^{-3}, and the residual of the energy equation fell below 10^{-6}.

Table 1
Material properties employed in DEM.

Materials	Density (kg/m^3)	Heat capacity (J/kg·K)	Thermal conductivity (W/m·K)	Viscosity (kg/m·s)
Concentrated H_2SO_4	1840	1390	0.8	0.00215
Intercalation compounds	2000	700	5	0.045
Glass	2500	1200	2.2	/

2.2.2. DEM model

In the DEM model, all particles within the computational domain are tracked using a Lagrangian approach. The translational and rotational motions of the particles are governed by the equations of motion, as defined in Eq. (5) and Eq. (6), respectively.

$$m_p \frac{\partial v_p}{\partial t} = F_p^C + m_p g + F_p^{f_p} \tag{5}$$

$$I_p \frac{\partial w_p}{\partial t} = T_p \tag{6}$$

V_p is the translational velocity of the particle, F_P^C is the contact force acting on the particle, and $F_p^{f_p}$ is the fluid-particle interaction force. I_p is the moment of inertia tensor of the particle, ω_p is the angular velocity, and T_p is the torque acting on the particle. The contact force consists of a force perpendicular to the contact surface and a tangential force, Eq. (7):

$$F_p^C = F_{p,n}^C + F_{p,t}^C \tag{7}$$

$F_{p,n}^C$ is the normal elastic-plastic contact force conducted on the particle, and $F_{p,t}^C$ is the tangential contact force. In this coupled approach, the governing equations for the fluid phase in Fluent remain applicable, and to ensure appropriate coupling, the term M_f in Eq. (2) is replaced by $F_p^{f_p}$, which represents the fluid-particle interaction force. This term captures the influence of fluid flow on particle motion. The pressure gradient force acting on the particle is given by Eq. (8):

$$F_{\nabla p} = -V_p \nabla p \tag{8}$$

$F_{\nabla p}$ is the pressure gradient force, and V_p is the volume of the particle. Based on probabilistic statistical theory, the Tavares breakage model is employed to describe the probability of particle fragmentation, Eq. (9).

$$P_b = 1 - \exp\left[-\frac{{\sigma_p}^m}{\sigma_0} \right] \tag{9}$$

σ_p is the maximum principal stress experienced by the particle, σ_0 is the characteristic stress threshold of the material, and m is the Weibull modulus, which reflects the uniformity of the strength distribution. The particle shape parameters are listed in Table 2, and appropriate particle injection rates are set according to different inlet velocities to ensure a consistent total particle count of 3721. The verification of the grid's independence is performed with detailed information provided in **Figure S2**.

2.3. RMD simulation

In this study, reactive molecular dynamics (RMD) simulations were employed to investigate interfacial reactions between multiple phases. The ReaxFF reactive force field developed by Zhang and Van Duin et al. was employed to study the oxidation mechanisms of both pristine and defect-containing graphene [36]. A pristine graphene sheet with dimensions of 22 Å × 15 Å and comprising 120 carbon atoms was constructed. A single-vacancy defect was introduced by removing one C atom, resulting in a 119-atom configuration. Geometry optimization and energy minimization were performed using the conjugate gradient algorithm, followed by a 100 ps relaxation at 5000 K to obtain a thermodynamically stable structure. Oxidation simulations were performed within the NVT ensemble after equilibration. The graphene sheet was centered in a simulation box of 22 Å × 15 Å × 11 Å, with 50 O_2 molecules randomly placed on both sides. Periodic boundary conditions were applied in the x and y directions to simulate an infinite surface, while non-periodic reflective boundaries were applied in the z direction to confine the gas molecules. Initial atomic velocities were assigned based on the Maxwell-Boltzmann distribution. Atomic charges were calculated using the charge equilibration method, updated every 10 steps to balance accuracy and computational efficiency. A time step of 0.1 fs was employed to capture the oxidation dynamics with high temporal resolution. Output data were recorded every 1000 steps, including the evolution of oxidation products determined via bond order analysis. The entire reaction proceeds through several key stages, illustrated in **Figure S3**. Upon the injection of reactants, the initial defect sites begin to expand, accompanied by the onset of oxygen atom grafting. As the reactants continue to flow through the heart-shaped microchannel, intensive grafting of O atoms occurs, initiating the disruption of the carbon layer from the center. This disruption gradually propagates toward the edges of the C layer, ultimately resulting in the cleavage of the carbon framework. A Python script based on the Pandas library was developed to extract species-specific data during the reaction process, including O_2, CO, CO_2, and other C/O clusters.

It is important to note that RMD simulations are intrinsically focused on capturing atomistic reaction mechanisms at the nanoscale and on the picosecond timescale, and are therefore incapable of directly replicating macroscopic flow behavior. The term "simulated flow rate" in this context should be regarded as a parameter reflecting the reaction advancement rate, used to modulate the interaction frequency and chemical reactivity between O_2 molecules and graphene. To align the RMD simulations with experimental microchannel conditions, five representative experimental flow velocities (0.025, 0.1, 0.25, 0.5, and 1.0 m/s) were correspondingly mapped to relative simulation velocities of 10, 40, 100, 200, and 400 m/s. This mapping maintains a consistent linear scaling ratio, thereby ensuring the comparability of reaction trends between molecular simulations and experimental results.

Table 2
The summary of the particle shape parameters.

Shape	Vertical aspect ratio	Horizontal aspect ratio	Sharp corner number	Superquadratic rate
Polyhedron	1.5	0.75	25	2

3. Results and discussions

3.1. Investigation of macroscopic flow behavior

The heating section at the inlet under different flow velocities is first studied. Given that the heating surface is identical in all cases and the inlet and outlet fluid temperatures remain constant, the heat flux (q) generated at the wall is thus positively correlated with the convective heat transfer coefficient (h), described by Eq. (10):

$$h = \frac{q}{T_{ave} - T_{f,\ ave}} \tag{10}$$

T_{ave} is the average temperature of the heated surface, and $T_{f,\ ave}$ is the average temperature of the fluid, calculated by $T_{f,\ ave} = \frac{T_{in}+T_{out}}{2}$, T_{in} and T_{out} are the inlet and outlet temperatures of the fluid, respectively.

The wall heat flux distribution is shown in Figs. 2a-e. Different scales are used to visualize the relative spatial distribution of wall heat flux at different inlet velocities. The convective heat transfer capacity of the fluid increases significantly with the increased inlet velocity. Notable enhancement is observed in the conical inlet section and the bifurcation region, which is attributed to the specifically designed geometry: diameter variations compress the fluid, accompanied by the enhanced shear effects and local pressure gradients. Moreover, the splitting and recombination structures in the heart-shaped region induce repeated stretching and lateral shearing of the fluid [37]. The heat flux along the sampling line is collected to facilitate a direct comparison of convective heat transfer performance under various inlet velocities, Fig. 2f. When the inlet flow rate is 1 m/s, the heat flux at the initial sampling site can reach 6.70×10^{-5} W/m^2. When the inlet flow rate is 0.025 m/s, the heat

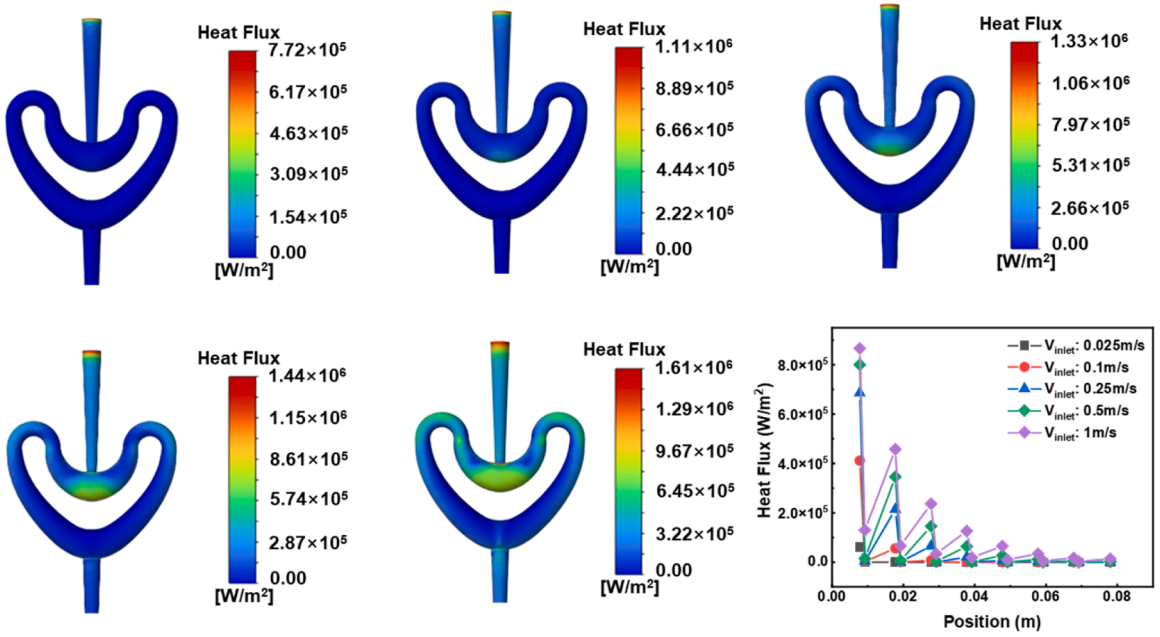

Fig. 2. The heat flux on the wall with V_{inlet} of (a) 0.025 m/s; (b) 0.1 m/s; (c) 0.25 m/s; (d) 0.5 m/s; and (e) 1 m/s; (f) Comparison of the surface heat flux distribution on the sampling line of various inlet velocities (the x-axis "position" refers to the sampling line drawn along the centerline of the microchannel wall surface, **Figure S2(b)**).

flux rate at the sampling site is almost zero. As the fluid temperature gradually approaches the wall temperature, the heat flux decreases toward zero, indicating a convergence in convective heat transfer performance [38]. This suggests that although local heat transfer intensity varies with flow rate, a well-designed channel ensures that the fluid temperature sufficiently approaches the wall temperature, enabling effective overall heat transfer.

The variation in fluid temperature during flow is compared, and the results are presented in Figs. 3a-e. The number of units required for the fluid to reach the intermediate reaction temperature can be determined. By comparing the initial units with larger temperature gradients, it is obvious that a significant temperature increase primarily occurs in the bifurcation region, which is consistent with the previous finding. The temperature distribution along the sampling line is shown in Fig. 3f, where the reaction temperature is reached sequentially in the 1st, 3rd, 5th, 6th, and 7th units as the inlet velocity increases. Based on the recorded residence time of particles, the corresponding reaction durations for the five cases are 133.37 s, 38.57 s, 18.57 s, 8.20 s, and 4.46 s, respectively. Compared to the widely adopted improved Hummers' method for synthesizing graphene oxide, the intermediate-temperature oxidation stage in this approach requires only ~0.5 h, representing more than a 13-fold reduction in processing time [12]. The particle temperature profiles along the flow path are shown in **Figure S4**, which shares the same trend as the fluid temperature.

The microchannel in this study is modeled as a series of variable-diameter circular tubes, and the radial velocity distribution in the microchannel follows Eq. (11):

$$u(r) = \frac{\Delta P}{4\mu L}\left(R^2 - r^2\right) \tag{11}$$

ΔP is the pressure drop, μ is the fluid viscosity, L is the length of the pipe, and R is the radius of the pipe. The fluid velocity distribution along the flow direction is shown in Figs. 4a-e. By comparing the velocity distributions at the sampling cross-section under different inlet velocities, it is

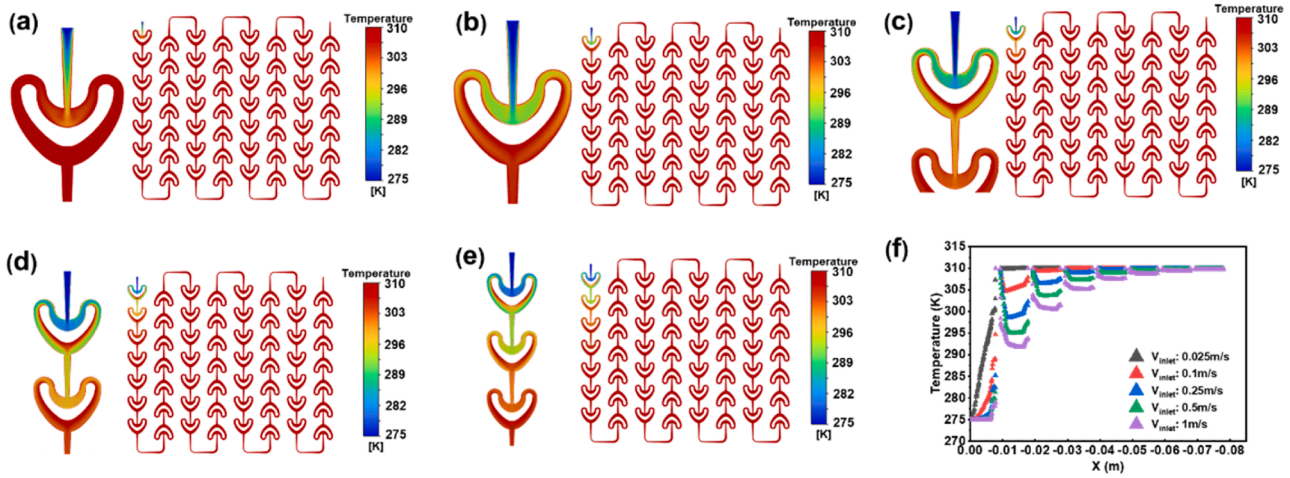

Fig. 3. Temperature distribution of the fluid with V_{inlet} of (a) 0.025 m/s; (b) 0.1 m/s; (c) 0.25 m/s; (d) 0.5 m/s; and (e) 1 m/s; (f) Comparison of the surface temperature on the sampling line of various inlet velocities.

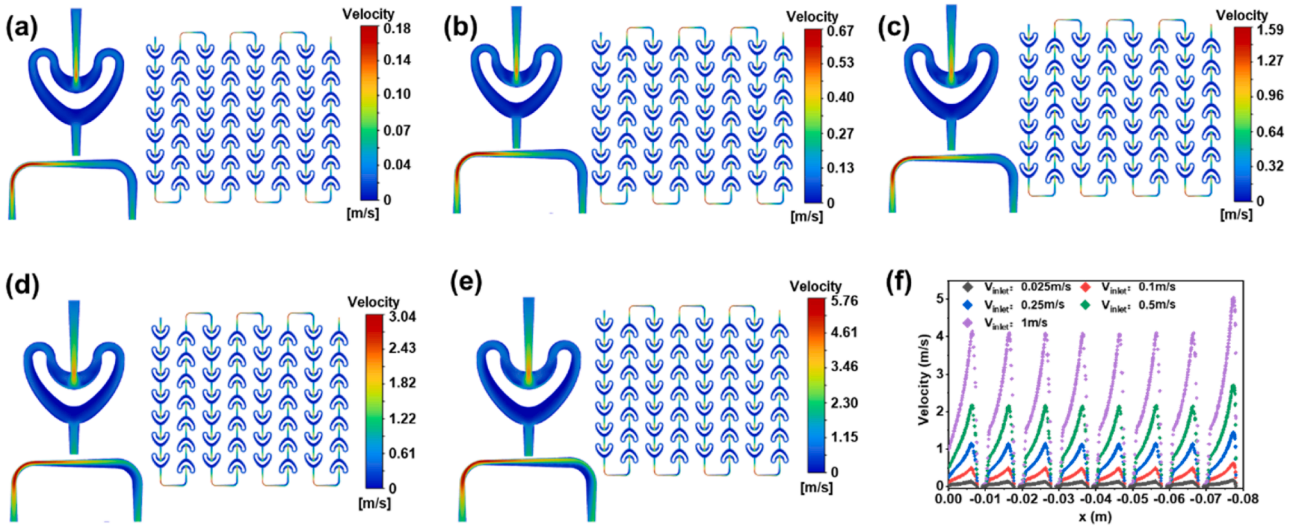

Fig. 4. Flow velocity distribution of the fluid with V_{inlet} of (a) 0.025 m/s; (b) 0.1 m/s; (c) 0.25 m/s; (d) 0.5 m/s; and (e) 1 m/s; (f) Comparison of the flow velocity distribution on the sampling line of various inlet velocities.

observed that the maximum velocity consistently occurs at the downstream end of the conical channel. This is attributed to the compression effect caused by the diameter reduction in the conical section. Fig. 4f compares the velocity profiles at the sampling location, showing that in a series of identical heart-shaped units, the velocity consistently follows the same variation pattern. The maximum velocity-increasing rates in the microchannel are 620 %, 570 %, 536 %, 508 %, and 476 %, respectively. This trend can be attributed to the nonlinear characteristics of laminar flow within confined geometries. At relatively low velocities, the conical and bifurcated structure of the microchannel introduces strong local pressure gradients and shear deformation, leading to more pronounced fluid acceleration. However, inertial effects begin to dominate as the inlet velocity increases, and the relative contribution of geometric features to flow acceleration becomes less significant [39]. Additionally, higher flow rates result in thinner boundary layers and more uniform velocity profiles, further reducing the sensitivity of maximum velocity enhancement. This suggests that the passive flow control capability of the microchannel geometry becomes saturated at elevated flow conditions, which is critical for optimizing design parameters in microfluidic applications targeting heat or mass transfer enhancement. The particle velocity exhibits a similar trend, **Figure S5**. Notably, as the inlet velocity increases, particles tend to gradually shift

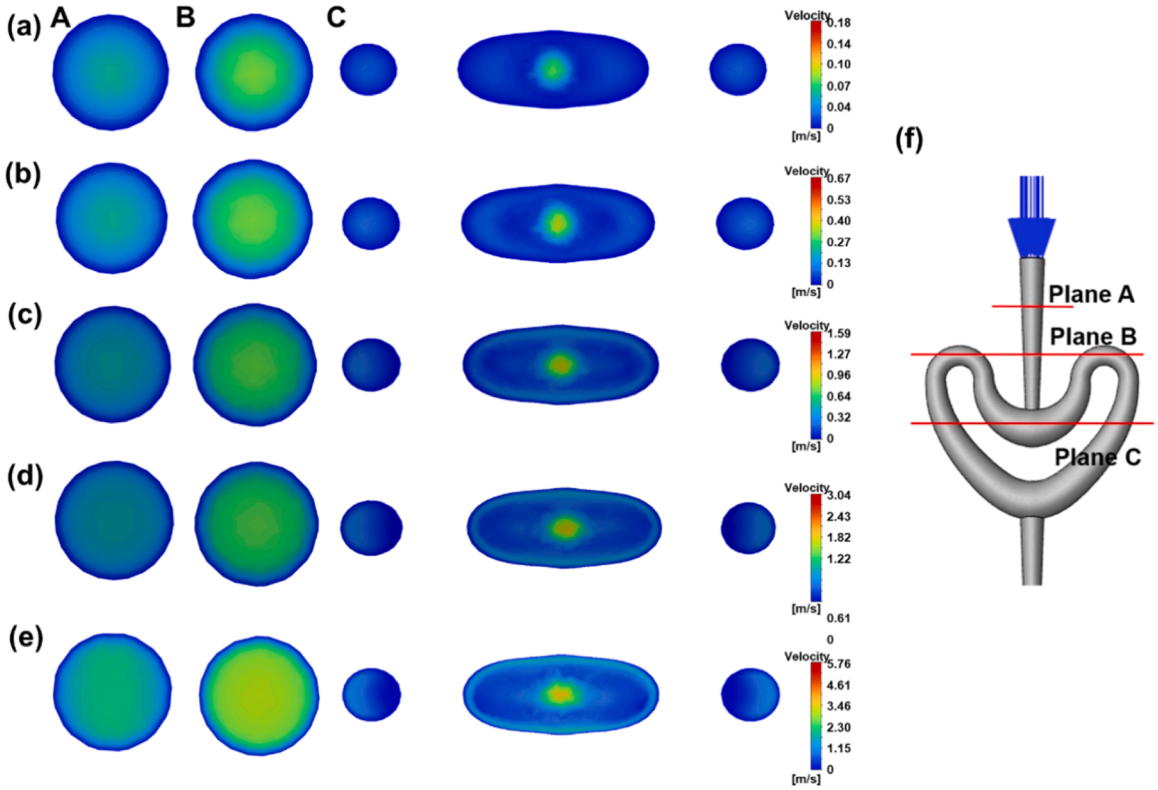

Fig. 5. Velocity distribution on the transverse section of the microfluidic channel with the V_{inlet} of (a) 0.025 m/s; (b) 0.1 m/s; (c) 0.25 m/s; (d) 0.5 m/s; and (e) 1 m/s; (f) Comparison of the flow velocity distribution on the sampling line of various inlet velocities.

toward one side of the heart-shaped units due to inertial effects and slight asymmetries in the microchannel geometry, rather than passing through uniformly, thereby increasing the risk of clogging.

A radial cross-section of the channel is selected, and three representative velocity profiles within the heart-shaped unit are investigated with the results presented in Figs. 5a-e. The cross-section locations are indicated in Fig. 5f. According to the Poiseuille theory for the laminar flow of Newtonian fluids in circular pipes [40], the shear rate distribution is given by Eq. (12):

$$\dot{\gamma}(r) = \frac{4V}{R^2} r \tag{12}$$

$\dot{\gamma}(r)$ is the shear rate at the radial position of r, V is the average velocity, and r is the radial distance from the center of the circular pipe. The velocity in the central region of the pipe increases significantly from 0.18m/s to 5.76 m/s with the increased inlet velocity, while the near-wall velocity is always close to zero, as shown in Figs. 6a-e. It leads to an increasing velocity gradient between the center and the wall, which in turn results in an elevated shear rate. The increased shear rate intensifies interlayer slip within the fluid, thereby enhancing the scouring effect and promoting both linear propulsion and rotational motion of suspended solid particles [41]. For Newtonian fluids, the shear stress and shear rate exhibit the following linear relationship, Eq. (13):

$$\tau = \mu\dot{\gamma} \tag{13}$$

μ is the dynamic viscosity of the fluid. As the shear rate increases, the shear force exerted by the fluid on the particles also increases, facilitating improved separation between particles and enhancing the overall reaction efficiency.

The realistic wall shear models under various velocities in microfluidic microchannels are presented in **Figure S6**. The maximum wall shear stress occurs at the downstream end of the conical section when the flow velocity is 1 m/s. The shear stress increases with the development of fluid flow within the channel, and its variation is closely correlated with the local velocity at the wall. This stress partially reflects the shear intensity between the fluid and the channel and can be used to predict potential clogging phenomena and channel wall erosion during flow.

3.2. Force analysis of the particle

To further investigate the relationship between microscale particle reaction kinetics and force field distribution, a high-fidelity numerical simulation was performed on the final heart-shaped microchannel unit that reached the required intermediate reaction temperature, using a bidirectionally coupled DPM and DEM. Particles are treated as discrete physical entities, whose motion is governed by multiple forces, including pressure gradient force, viscous drag, inter-particle contact force [42], and fluid inertia. The DPM resolves the influence of the fluid field on particle motion by tracking particle trajectories within the Euler-Lagrange framework, while the DEM accounts for inter-particle interactions such as collision, rolling, and friction, thereby capturing a more realistic representation of microscale transport processes. The mechanical data of particles throughout their traversal of the unit were recorded and analyzed. Figs. 6a-e present the temporal evolution of the maximum and minimum pressure gradient forces experienced by particles during the flow process. The four vertical dashed lines in the figures correspond to key event points: (i) particle entry into the bifurcated region, (ii) complete particle entry, (iii) partial particle exit, and (iv) complete particle exit. These events effectively divide the particle motion into distinct stages and facilitate analysis of the spatiotemporal evolution of particle-force interactions. From the mechanical response perspective, the pressure gradient force on the particles rises sharply during the initial entry stage into the bifurcated region, indicating a strong driving force induced by fluid streamline bending and local acceleration. Once all particles have fully entered the structure, the minimum pressure gradient force rises to a non-zero value, suggesting that the particles remain continuously subjected to external forces, without stagnation or retention. This observation confirms the capacity of the specific structure to maintain a persistent force field acting on the particles throughout their passage.

It is important to emphasize that the pressure gradient force not only governs the velocity distribution and trajectory evolution of particles within the microchannel but also directly influences their relative motion. This affects the interfacial area and the spatial distribution of chemical reactions in turn. It has been reported that the pressure gradient force is one of the key physical mechanisms responsible for forming efficient mixing zones, enhancing mass transfer flux, and accelerating local reaction rates in microscale multiphase flow systems [43,44]. The maximum value of the average pressure gradient force is

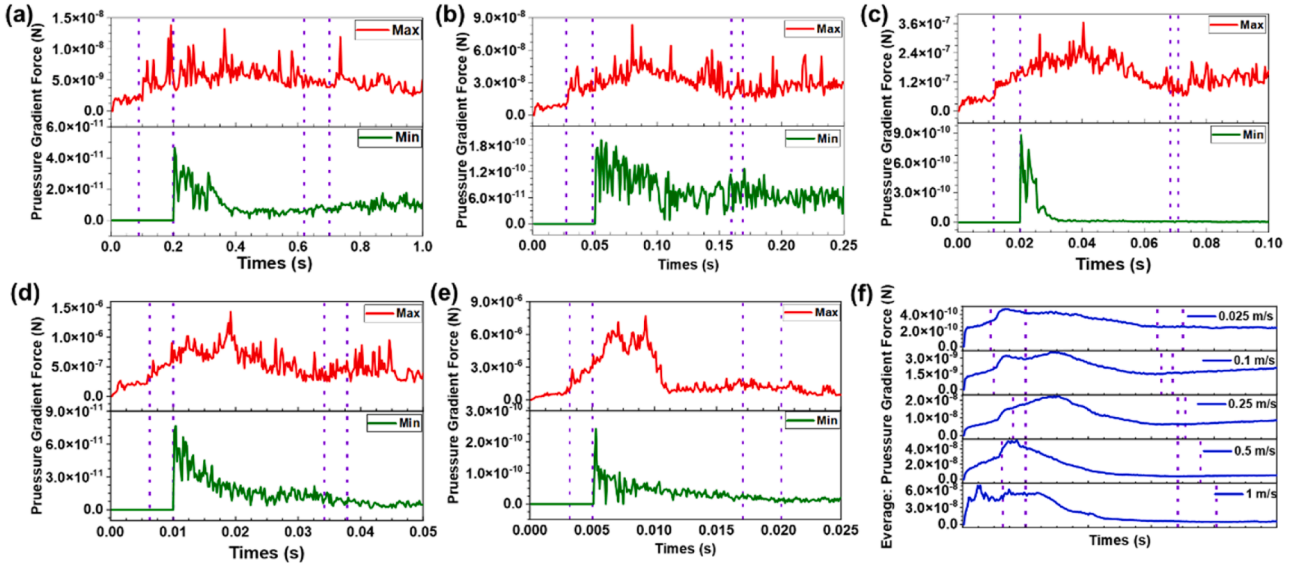

Fig. 6. Statistics of the maximum/minimum pressure gradient force experienced by all particles as they flow through the microfluidic channel with the V_{inlet} of (a) 0.025 m/s; (b) 0.1 m/s; (c) 0.25 m/s; (d) 0.5 m/s; and (e) 1 m/s; (f) Everage pressure gradient force experienced by all particles as they flow through the microfluidic unit with various inlet velocities.

summarized in Fig. 6f. With the increase of the inlet flow velocity, the positions where the peak value of the pressure gradient force occurs are the same, reaching the highest when the particles enter the heart-shaped bifurcation part, demonstrating the enhancing effect of this structural design on mass transfer. Notably, with increasing inlet flow velocity, the maximum pressure gradient force exhibits a monotonic rise, whereas the minimum counterpart displays a non-monotonic trend. This behavior is primarily attributed to the reconstruction of local flow fields within the heart-shaped microchannel. At intermediate velocities (0.25–0.5 m/s), the bifurcation-recombination regions are more susceptible to recirculation and flow separation, leading to intensified local adverse pressure and consequently more negative pressure gradient forces. In contrast, at higher velocities (1.0 m/s), the enhanced kinetic energy of the mainstream suppresses the development of recirculation zones, resulting in a reduced absolute value of the local minimum. This transition highlights the nonlinear interplay between shear-dominated and inertia-dominated transport mechanisms within the microchannel.

3.3. Microscopic bond breaking and formation investigation via RMD

Figs. 7a-e show the temporal evolution of the O/C ratio during the oxidation of graphite under five distinct simulated flow velocity conditions via RMD. Based on the slope transitions and inflection points of the O/C curves, in conjunction with abrupt changes in reaction rate, the oxidation process can be categorized into three distinct stages. Stage I (blue region) corresponds to the initial phase, characterized by physical adsorption and preliminary dissociation of oxygen molecules on the graphite surface or defect sites. Due to a relatively high kinetic barrier, the O/C ratio increases slowly, indicating an induction period. Stage II (red region) marks a significant acceleration in the reaction rate, during which extensive cleavage of C—C bonds occurs, creating numerous reactive vacancies. The oxidation proceeds intensively with copious formation of C—O and $C = O$, leading to a sharp increase in the O/C ratio. Stage III (green region) represents the saturation stage, where the O_2 concentration decreases. The system transitions to secondary reactions predominantly involving $C = O$ formation, with a gradual decline in reaction rate and a plateau in the O/C curve. The evolution of the O/C curves under varying flow rates reveals substantial shifts in the temporal distribution of each reaction stage as the flow velocity increases. As the reaction proceeds, the oxidant is nearly depleted, leading the system into a regime dominated by thermally induced structural fluctuations. In this period, C—C bond cleavage occurs infrequently, and the process is primarily governed by the scattering and recombination of C—O chain segments. These transformations involve the dynamic association and dissociation of basic C—O species, including CO, CO_2, and various C—O clusters, reflecting the intrinsic thermodynamic behavior of a highly disordered carbonaceous matrix. Fig. 7f provides a quantitative comparison of the temporal proportions of each stage under different flow velocities. It indicates that at lower flow velocities, Stage III dominates the oxidation timeline: for instance, at the lowest velocity (10 m/s), it accounts for up to 46 %, whereas at the highest velocity (400 m/s), its proportion contracts sharply to only 16 %. This suggests that under low flow conditions, O_2 exhibits prolonged residence times on the graphite surface, enhancing its interaction at defect sites and facilitating deeper oxidation, ultimately resulting in higher oxidation degrees (e.g., O/C ratio up to 0.43). In contrast, at high flow velocities, O_2 swiftly passes over the graphite surface and is expelled before sufficiently engaging in the reaction, leading to premature termination and significantly reduced oxidation levels (with O/C ratio as low as 0.28). Notably, the relative proportion of Stage II increases with flow velocity, indicating that oxidation reactions become more temporally concentrated and exhibit strong transient reactivity at high flow rates. However, due to limited subsequent reaction time, the final oxygen incorporation remains lower. Therefore, the ultimate oxidation extent is governed by the combined effects of flow velocity and O_2 residence time.

3.4. Experimental characterization of the synthesized GO

XPS is performed to investigate the effect of flow rate on the oxidation degree of the synthesized GO. Fig. 8a presents the wide-scan XPS spectra, where two dominant peaks corresponding to C 1 s and O 1 s are observed at approximately 285 eV and 532 eV, respectively. At the low flow rate of 0.025 m/s, the O/C ratio is approximately 0.44, attributed to the prolonged contact time between the oxidant and graphite flakes within the microchannel, which facilitates more efficient grafting of oxygen-containing functional groups. In contrast, at the high flow rate of 1.0 m/s, the O/C ratio decreases to approximately 0.21 due to the reduced residence time, which limits the extent of oxidation and decreases oxygen incorporation efficiency. The tunable range of oxidation could reach up to 110 %, markedly surpassing that of vortex-focusing

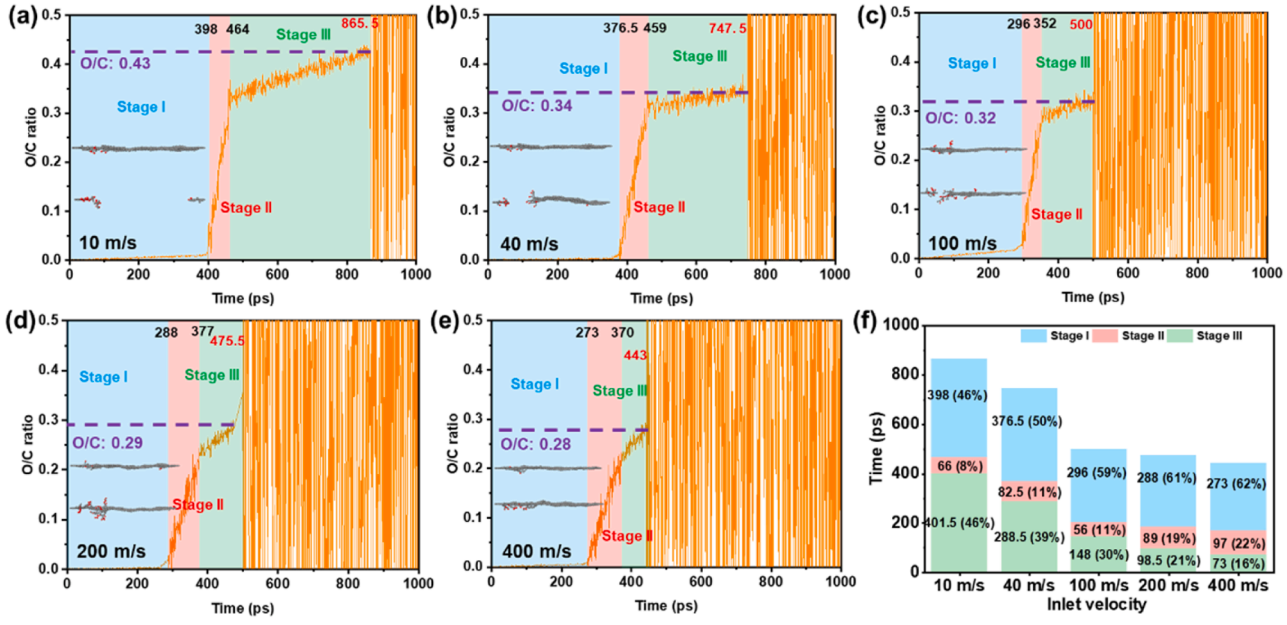

Fig. 7. Temporal evolution of the O/C ratio on the graphite surface under simulated O_2 flow velocities of (a) 10 m/s, (b) 40 m/s, (c) 100 m/s, (d) 200 m/s, and (e) 400 m/s by RMD; (f) Comparative analysis of the time fractions associated with each reaction stage under different simulated O_2 flow velocities.

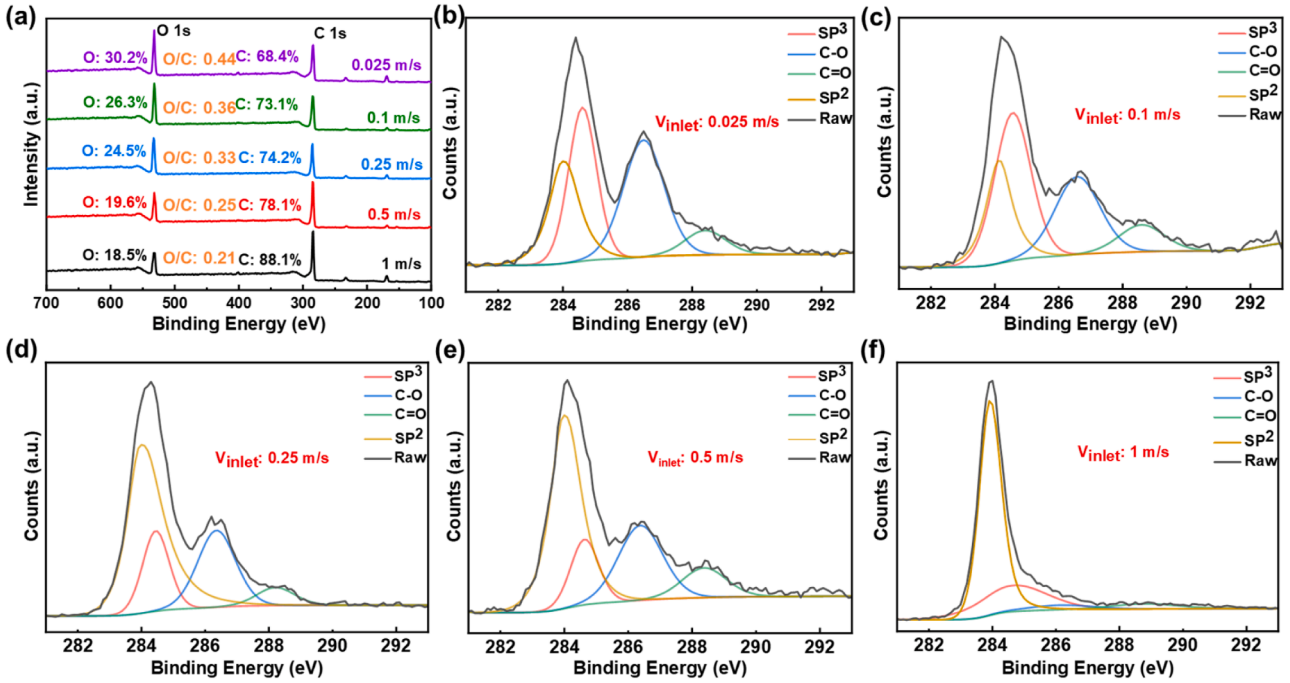

Fig. 8. (a) XPS wide scan spectra of synthesized GO with various inlet flow rates; High-resolution C 1 s spectra of GO with various inlet flow rates: (a) 1 m/s; (b) 0.5 m/s; (c) 0.25 m/s; (d) 0.1 m/s; and (e) 0.025 m/s.

devices (±5 % variation in liposome synthesis, Ref. [22]) and blade-type channels (constrained regulation efficiency in MOF synthesis, Ref. [21]). The oxidation data in XPS characterization show a similar trend with the RMD simulation results, supporting the validity of the proposed multiphysics-multiscale simulation strategy. Figs. 8b-f present high-resolution C 1 s spectra fitted under various flow conditions, revealing the relative contents of different carbon species in the GO structure. The spectra primarily include five carbon components corresponding to distinct chemical environments: sp^2-hybridized C (~283.9 eV), sp^3-hybridized C (~284.8 eV), C—O (~286.1 eV), and $C = O$ (~288.4 eV). The fitting results indicate that decreasing the flow rate enhances the intensity of oxygen-containing groups such as C—O and $C = O$, while the proportion of sp^2-hybridized carbon decreases, confirming that lower flow rates favor surface oxidation and functionalization of graphene sheets. Notably, the C—O content exhibits a gradual increase with longer residence times, whereas the $C = O$ content shows an irregular trend. This can be attributed to the shear forces and turbulent vortices within the microchannel, which promote uniform oxidant penetration and facilitate the homogeneous formation of C—O groups. However, $C = O$ groups are typically located at the edges of graphene sheets, where carbon atoms are less abundant and more readily saturated by oxidation in the early stages. As a result, their subsequent growth is limited, leading to discontinuous or non-monotonic changes in their relative content.

At the flow velocity of 1.0 m/s, the O/C ratio predicted by the RMD simulations is 0.28, whereas the XPS measurement yields a value of 0.21, resulting in a deviation of approximately 25 %. This discrepancy primarily arises from the simulation's omission of the edge-carbon saturation effect in graphene. High-resolution C 1 s spectra (Fig. 8c) confirm that $C = O$ preferentially occupy edge sites under low flow conditions, accounting for 28 % of the total carbon species, thereby restricting further oxidation during the recombination stage (a condition that is not adequately represented in the current RMD simulations). Despite this deviation, the simulation framework effectively captures the overall trend and mechanism of flow-induced oxidation, validating its utility in guiding microfluidic reaction system design.

4. Conclusions

To sum up, a heart-shaped microchannel was designed and successfully employed for the rapid and controllable synthesis of GO with tunable oxidation degrees. The intermediate-temperature oxidation stage in this method only takes approximately 0.5 h, which is over 13 times shorter than the processing time of the traditional strategy. By adjusting the inlet flow rate, experimental results revealed a strong correlation between the O/C ratio of the product and the residence time, confirming the significant role of channel geometry in flow regulation and reaction control. A multiscale-multiphysics strategy was established, enabling cross-scale modeling from macroscopic fluid dynamics to microscale reaction pathways. As the inlet velocity increased from 0.025 m/s to 1.0 m/s, the wall heat flux within the microchannel was significantly enhanced (with a maximum value up to 6.70×10^{-5} W/m^2), and the centerline velocity increased to 5.76 m/s. The conical inlet and heart-shaped bifurcation regions induced pronounced shear and mixing effects, thereby promoting heat transfer and reactant contact efficiency. Under high flow conditions, the resulting interlayer stresses were sufficient to induce graphite flake exfoliation and increase the exposed reactive surface area. The O/C ratios obtained from RMD simulations (0.43–0.28) show good agreement in trend with XPS measurements (0.44–0.21), confirming the consistency between predicted and experimental oxidation behavior. The deviation mainly arises from the simulation's omission of edge-carbon saturation effects, leading to an overestimation of reoxidation in the later stages. This study systematically elucidates the role of heart-shaped microchannel geometry in the controllable synthesis of graphene oxide from three perspectives: structural design, cross-scale simulation, and experimental validation. While the current work focuses on GO synthesis, the proposed framework can be extended to reactions such as exfoliation, hydrothermal growth, or crystallization. Future efforts will focus on local field validation and integration with real-time sensing technologies.

CRediT authorship contribution statement

Yifan Li: Writing – original draft, Funding acquisition,

Conceptualization, Investigation. **Xiaojun Xiong:** Methodology, Data curation. **Hongao Yang:** Formal analysis. **Wei Yu:** Supervision. **Bingyang Cao:** Writing – review & editing, Supervision, Funding acquisition.

Declaration of competing interest

The authors declare that they have no known competing financial interests or personal relationships that could have appeared to influence the work reported in this paper.

Acknowledgments

The authors acknowledge funding from the National Natural Science Foundation of China (52306214, 52425601), the Shanghai Chenguang Plan Program (22CGA78), and the National Key Research and the Development Program of China (No. 2023YFB4404104).

Supplementary materials

Supplementary material associated with this article can be found, in the online version, at doi:10.1016/j.ijheatmasstransfer.2025.127802.

Data availability

Data will be made available on request.

References

[1] W. Waheed, S. Anwer, M. Umair Khan, M. Sajjad, A. Alazzam, 2D $Ti_3C_2T_x$-MXene nanosheets and graphene oxide based highly sensitive humidity sensor for wearable and flexible electronics, Chem. Eng. J. 480 (2023) 147981, https://doi.org/10.1016/j.cej.2023.147981.
[2] X. Yi, W. He, X. Zhang, K.S. Hui, W. Xu, Biomass-derived mesoporous core-shell Fe3C@graphene oxide nanospheres for electrochemical energy storage, Int. J. Hydrogen Energy 64 (25) (2024) 448–454, https://doi.org/10.1016/j.ijhydene.2024.03.311.
[3] L. Amiri-Zirtol, H. Emtiazi, S.N. Abootalebi, A. Gholami, Dual acid-base catalysis with biologically modified graphene oxide: a sustainable route to polyhydroquinolines with antimicrobial properties, Sci. Rep. 15 (2025) 10194, https://doi.org/10.1038/s41598-025-94389-0.
[4] M. K M, J.J. Vijaya, A.J.P. Paul Winston, K. Akash, P. Sagayaraj, S. Rajeshkumar, M.K. Al-Sadoon, Untapped potential: sugarcane bagasse to biocompatible graphene oxide as biomedicine, Diam. Relat. Mater. 148 (2024) 111479, https://doi.org/10.1016/j.diamond.2024.111479.
[5] J. Chen, L. Li, Effect of oxidation degree on the thermal properties of graphene oxide, J. Mater. Res. Technol. 9 (6) (2020) 13740–13748, https://doi.org/10.1016/j.jmrt.2020.09.092.
[6] M. Tavakol, A. Montazeri, S.H. Aboutalebi, R. Asgari, Mechanical properties of graphene oxide: the impact of functional groups, Appl. Surf. Sci. 525 (2020) 146554, https://doi.org/10.1016/j.apsusc.2020.146554.
[7] W. Wang, Y. Zhang, S. Liu, W. Wu, X. Du, Study on thermal property improvement of MOF material UiO-66 with surface modification by graphene oxide, Int. J. Heat Mass Transf. 239 (2025) 126588, https://doi.org/10.1016/j.ijheatmasstransfer.2024.126588.
[8] A. Gutiérrez-Cruz, A.R. Ruiz-Hernández, J.F. Vega-Clemente, D.G. Luna-Gazcón, J. Campos-Delgado, A review of top-down and bottom-up synthesis methods for the production of graphene, graphene oxide and reduced graphene oxide, J. Mater. Sci. 57 (2022) 14543–14578, https://doi.org/10.1007/s10853-022-07514-z.
[9] W.S. Hummers Jr, R.E. Offeman, Preparation of graphitic oxide, J. Am. Chem. Soc. 80 (6) (1958) 1339, https://doi.org/10.1021/ja01539a017.
[10] D.C. Marcano, D.V. Kosynkin, J.M. Berlin, A. Sinitskii, Z. Sun, A. Slesarev, L. B. Alemany, W. Lu, J.M. Tour, Improved synthesis of graphene oxide, ACS Nano 4 (8) (2010) 4806–4814, https://doi.org/10.1021/nn1006368.
[11] N.M. Huang, H.N. Lim, C.H. Chia, M.A. Yarmo, M.R. Muhamad, Simple room-temperature preparation of high-yield large-area graphene oxide, Int. J. Nanomedicine 6 (2011) 3443–3448, https://doi.org/10.2147/IJN.S26812.
[12] J. Chen, B. Yao, C. Li, G. Shi, An improved Hummers method for eco-friendly synthesis of graphene oxide, Carbon 64 (2013) 225–229, https://doi.org/10.1016/j.carbon.2013.07.055.
[13] L. Liu, M. Wang, H. Shen, Thermal-dynamic study on the novel designed double-layer impinging jet microchannel heat sinks with horizontal and inclined fins verified by additive manufacturing technology, Appl. Therm. Eng. 269 (2025) 126185, https://doi.org/10.1016/j.applthermaleng.2025.126185.
[14] W. Sun, P. Li, T. Zhou, Y. Li, C. Li, X. Shao, H. Shen, Thermo-fluids performance analysis and experimental verification of topologically optimized mini-channel heat sinks integrated with impact jet, Int. J. Therm. Sci. 211 (2025) 109705, https://doi.org/10.1016/j.ijthermalsci.2025.109705.
[15] Y. Zhuo, P. Li, G. Hou, R. González, H. Shen, Numerical analysis on working conditions of the novel design combining double-layer nested microchannel and central impact jets verified by 3D printing technology, Int. J. Heat Mass Transf. 240 (2025) 126669, https://doi.org/10.1016/j.ijheatmasstransfer.2025.126669.
[16] X.Lan H.Shen, G. Xie, C. Wang, Parametric study for thermal uniformity analysis on vertical fin located in novel designed impacting-jet double-layer nested microchannel heat sinks verified by SLM 3D printing method, Int. Commun. Heat Mass Transf. 159 (2024) 108321, https://doi.org/10.1016/j.icheatmasstransfer.2024.108321.
[17] H. Shen, P. Li, L. Liu, M. Rosales-Vera, S. Zheng, Novel design and thermal-dynamic analysis on impact-jet nested double-layer microchannel heat sinks with streaming block, Appl. Therm. Eng. 251 (2024) 123496, https://doi.org/10.1016/j.applthermaleng.2024.123496.
[18] H. Shen, S. Gao, X. Lan, H. Liu, G. Xie, C. Wang, Performance of impingement-jet double-layer nested microchannel heat sinks with vertical central bifurcation–A numerical approach and experimental verification, Int. J. Heat Mass Transf. 222 (2024) 125203, https://doi.org/10.1016/j.ijheatmasstransfer.2024.125203.
[19] F. Tian, L. Cai, C. Liu, J. Sun, Microfluidic technologies for nanoparticle formation, Lab. Chip 3 (22) (2021), https://doi.org/10.1039/D1LC00812A.
[20] J.6. Shen, M. Shafiq, M. Ma, H. Chen, Synthesis and surface engineering of inorganic nanomaterials based on microfluidic technology, Nanomaterials 10 (6) (2020) 1177, https://doi.org/10.3390/nano10061177.
[21] N. Lee, S. Wiegand, Thermal design of a non-isothermal microfluidic channel for measuring thermophoresis, Int. J. Heat Mass Transf. 231 (2024) 125871, https://doi.org/10.1016/j.ijheatmasstransfer.2024.125871.
[22] C. Zhu, H. Guo, C. Chu, T. Fu, Y. Ma, Gas-liquid distribution and mass transfer of CO_2 absorption into sodium glycinate aqueous solution in parallel multi-channel microreactor, Int. J. Heat Mass Transf. 157 (2020) 119943, https://doi.org/10.1016/j.ijheatmasstransfer.2020.119943.
[23] G. Hao, Y.Chen C.Yu, X. Liu, Y. Chen, Controlled microfluidic encapsulation of phase change material for thermo-regulation, Int. J. Heat Mass Transf. 190 (2022) 122738, https://doi.org/10.1016/j.ijheatmasstransfer.2022.122738.
[24] L. Lyu, G. Hao, Y. Wang, Y. Chen, Y. Chen, X. Liu, Microfluidic fabrication of compound microfibers encapsulating nano-enhanced phase change material (PCM) for thermal regulation, Int. J. Heat Mass Transf. 233 (2024) 126052, https://doi.org/10.1016/j.ijheatmasstransfer.2024.126052.
[25] S. Rafique, S. Bashir, R. Akram, A. Mehmood, J.S. Khan, Z. Haq, M. Idrees, Green-microfluidics synthesis of thermally stable silver–chitosan composites for antibacterial activity, Chem. Papers 76 (2022) 3879–3889, https://doi.org/10.1007/s11696-022-02144-w.
[26] E.S. Szalai, J. Kukura, P.E. Arratia, F.J. Muzzio, Effect of hydrodynamics on reactive mixing in laminar flows, AIChE J. 49 (1) (2003) 168–179, https://doi.org/10.1002/aic.690490115.
[27] J.-O. Kim, W.-T. Koo, H. Kim, C. Park, T. Lee, C.A. Hutomo, S.Q. Choi, D.S. Kim, I.-D. Kim, S. Park, Large-area synthesis of nanoscopic catalyst-decorated conductive MOF film using microfluidic-based solution shearing, Nat. Commun. 12 (2021) 4294, https://doi.org/10.1038/s41467-021-24571-1.
[28] J.Y. Han, J.N. La Fiandra, D.L. DeVoe, Microfluidic vortex focusing for high throughput synthesis of size-tunable liposomes, Nat. Commun. 13 (2022) 6997, https://doi.org/10.1038/s41467-022-34750-3.
[29] Y. Chai, Y. Wang, B. Li, W. Qi, R. Su, Z. He, Microfluidic synthesis of lignin/chitosan nanoparticles for the pH-responsive delivery of anticancer drugs, Langmuir 37 (23) (2021) 7219–7226, https://doi.org/10.1021/acs.langmuir.1c00778.
[30] E. Livak-Dahl, I. Sinn, M. Burns, Microfluidic chemical analysis systems, Annu. Rev. Chem. Biomol. Eng. 2 (1) (2011) 325–353, https://doi.org/10.1146/annurev-chembioeng-061010-114215.
[31] Z. Wei, Y. Li, R.G. Cooks, X. Yan, Accelerated reaction kinetics in microdroplets: overview and recent developments, Annu. Rev. Phys. Chem. 71 (2020) 31–51, https://doi.org/10.1146/annurev-physchem-121319-110654.
[32] G.Q. Wang, J.R. Ni, The kinetic theory for dilute solid/liquid two-phase flow, Int. J. Multiphase Flow 17 (2) (1991) 273–281, https://doi.org/10.1016/0301-9322(91)90020-4.
[33] M. Sommerfeld, Numerical methods for dispersed multiphase flows, particles in flows, (2017) 327–396, https://doi.org/10.1007/978-3-319-60282-0_6.
[34] N.S. Weerasekara, M.S. Powell, P.W. Cleary, L.M. Tavares, M. Evertsson, R. D. Morrison, J. Quist, R.M. Carvalho, The contribution of DEM to the science of comminution, Powder Technol. 248 (2013) 3–24, https://doi.org/10.1016/j.powtec.2013.05.032.
[35] A.E. Kamholz, P. Yager, Theoretical analysis of molecular diffusion in pressure-driven laminar flow in microfluidic channels, Biophys. J. 80 (1) (2001) 155–160, https://doi.org/10.1016/S0006-3495(01)76003-1.
[36] A.C.T. van Duin, S. Dasgupta, F. Lorant, W.A. Goddard, ReaxFF: a reactive force field for hydrocarbons, J. Phys. Chem. A 105 (41) (2001) 9396–9409, https://doi.org/10.1021/jp004368u.
[37] W. He, C. Zhu, T. Fu, X. Gao, Y. Ma, H.Z. Li, The dynamics of bubble breakup in heart-shaped microchannels: effect of structure, Chem. Eng. J. 470 (2023) 144302, https://doi.org/10.1016/j.cej.2023.144302.
[38] S. Wu, Y. Chen, Y. Li, D. Zeng, Exergy transfer characteristics of forced convective heat transfer through a duct with constant wall heat flux, Energy 32 (5) (2007) 686–696, https://doi.org/10.1016/j.energy.2006.04.013.
[39] H. Amini, W. Lee, D. Di Carlo, Inertial microfluidic physics, Lab. Chip 14 (15) (2014) 2739–2761, https://doi.org/10.1039/C4LC00128A.

[40] K. Dutkowski, Experimental investigations of Poiseuille number laminar flow of water and air in minichannels, Int. J. Heat Mass Transf. 51 (25–26) (2008) 5983–5990, https://doi.org/10.1016/j.ijheatmasstransfer.2008.04.070.
[41] M.A. Tehrani, An experimental study of particle migration in pipe flow of viscoelastic fluids, J. Rheol. 40 (1996) 1057–1077, https://doi.org/10.1122/1.550773.
[42] C. Thornton, Granular dynamics, contact mechanics and particle system simulations, A DEM study, Particle Technol. Ser. 24 (2015), https://doi.org/10.1007/978-3-319-18711-2.
[43] H.A. Stone, A.D. Stroock, A. Ajdari, Engineering flows in small devices: microfluidics toward a lab-on-a-chip, Annu. Rev. Fluid Mech. 36 (1) (2004) 381–411, https://doi.org/10.1146/annurev.fluid.36.050802.122124.
[44] C.N. Baroud, F. Gallaire, R. Dangla, Dynamics of microfluidic droplets, Lab. Chip 10 (16) (2010) 2032–2045, https://doi.org/10.1039/C001191F.